

Synthesis and transport properties of epitaxial Bi (111) films on GaAs (111) substrates

Jagannath Jena¹, Eugene D. Ark¹, Siddhesh Ambhire², Michael D. Smith¹, Justin S. Wood¹, Junyi Yang¹, John Pearson¹, Hanu Arava¹, Daniel Rosenmann³, Ulrich Welp¹, Jidong S. Jiang¹, Deshun Hong¹, Ivar Martin¹, Steven S.-L. Zhang², and Anand Bhattacharya^{1*}

¹Material Science Division, Argonne National Laboratory, Lemont, Illinois 60439, USA

²Department of Physics, Case Western Reserve University, Cleveland, Ohio 44106, USA

³Center for Nanoscale Materials, Argonne National Laboratory, Lemont, Illinois 60439, USA

In recent decades, the growth of ultrathin epitaxial bismuth (Bi) films on various substrates has garnered interest due to their unique electronic properties. We report upon the growth and electrical transport properties of epitaxial Bi (111) films in the thickness range of 5-32 nm deposited directly on GaAs (111) substrates, without a buffer layer. The quality of Bi films is found to depend on conditions for substrate treatment using Ar⁺ ion-milling and annealing. Substrates milled at low ion beam currents display poor surface reconstruction after annealing, which hinders the growth of high-quality films. In contrast, substrates milled under optimized conditions led to reconstructed surfaces upon annealing, resulting in epitaxial Bi films with predominantly single-domain orientation. Although epitaxial films formed in both cases, transport measurements indicated significantly higher conductivity for films grown on optimally treated substrates. Measurements at low temperatures suggest that the transport properties are dominated by a surface state with high mobility electrons. Magneto-transport measurements suggest that conductivity and mobility improve progressively with increasing film thickness. For the thinnest 5 nm film, a hole-like state emerges, presumably as the electron-like state is gapped out. These results provide a robust methodology for growing high-quality epitaxial Bi films on GaAs (111) and offer insights into their unique transport properties, and our ability to tune them.

*anand@anl.gov

Elemental bismuth (Bi) is a unique semi-metal with notable characteristics such as a very low carrier density, small effective mass, and long mean free paths for charge carriers. Bi has a rhombohedral unit-cell and its electronic structure consists of three small ellipsoidal electron pockets at the L -points and one small hole pocket at the T -point in the Brillouin zone^{1,2}. However, it is known that in Bi films in the ultra-thin limit, the reduced dimensionality gaps out the bulk states due to quantum confinement³, and entirely distinct structural and electronic properties can emerge in the 2D limit, including the quantum spin Hall effect⁴, ferroelectricity⁵, and the potential for ideal 2D topological insulators⁶. Therefore, there is increasing interest in the development of high-quality crystalline thin films of bismuth, which has led to efforts to grow them on various substrates, including sapphire⁷, pyrolytic graphite⁸, InSb⁹, glass¹⁰, mica¹¹, Ge (111)¹², and different reconstructed surfaces of Si (111)^{11,13,14}. Of particular interest are thin films of Bi (111) (rhombohedral indexing, equivalent to Bi (0001) in hexagonal indexing), Fig. 2(a)), whose spin-split surface states have been studied extensively for their fundamental properties¹⁵⁻²⁴, and which in the limit of a single Bi bilayer²⁵ are predicted to host quantum spin Hall edge states with a large bulk gap²⁶. In thicker films and bulk single crystals, the two branches of the spin-split surface states of Bi (111) lead to a hexagonal electron pocket around the Γ -point, six teardrop-shaped hole pockets along the $\Gamma - M$ direction, and six needle-like electron pockets near the M -point. For films with thickness in the range of a few nanometers, angle-resolved photoemission spectroscopy (ARPES) measurements have shown that bulk states are progressively gapped away from the Fermi surface with reduced thickness²³. Furthermore, the degeneracy between the spin-split states near the M -point, or lack thereof, has been the subject of several studies, and the possible topological nature of these states is still debated^{21,22,27}. However, achieving the correct structural phase in large area epitaxial Bi (111) films in the 1-50 nm thickness range on insulating substrates

remains challenging, as the growth kinetics often do not favor the desired phase, leading instead to island-like morphology and the presence of secondary phases like Bi (110) crystallites⁷ (Bi (1012) in hexagonal indices).

In this study, we present a technique for growing high-quality epitaxial Bi films on GaAs (111) substrate at room temperature using molecular beam epitaxy. Our results demonstrate that thorough Argon ion milling to remove native oxide layers combined with high-temperature annealing of the substrate is essential for achieving the correct phase of the epitaxial Bi films. When the substrate's surface reconstruction is carefully optimized, the grown Bi films exhibit smooth surfaces with large, preferentially unidirectional domains, leading to high-quality epitaxial structure. These films show significantly enhanced mobility and higher magnetoresistance compared to those grown on poorly reconstructed substrates. For Bi films with thickness in the 15-32 nm range grown on optimized substrates, a high mobility electron pocket dominates transport properties at low temperatures, while for films in the 5-10 nm thickness range, a dominant hole-type carrier contribution is observed.

Experimental detail, results and discussion

Crystalline elemental films play an important role in modern technology²⁸⁻³² as well as in fundamental explorations^{33,34} of quantum matter. On an appropriate substrate, a rule of thumb for growth of crystalline elemental films is that the growth temperature (in K) is about 0.25-0.5 of the melting point of the element, though there are exceptions³⁵. In this study, we reported the layer-by-layer growth of elemental Bi (111) films, at room temperature on top of GaAs (111) substrates. The detailed substrate preparation and growth process are outlined below.

The treatment of the substrate prior to Bi growth is particularly important, as it significantly enhances the magneto-transport properties. The GaAs (111) substrate is first sonicated in acetone and then in isopropanol, each for 5 minutes, before being placed in the ion milling chamber to remove the native oxide layer and achieve a smooth surface. Two substrates (S#1 and S#2) were milled separately, using different ion beam currents in a background pressure of Argon gas of approximately 1.4×10^{-4} Torr. The Ar^+ ion beam is incident at approximately 45° , with $V_{\text{Beam}} = 600$ V and $V_{\text{Acc}} = 48$ V. Sample S#1 was first milled with an ion beam current of 16 mA for 90 seconds. After this initial milling step, the ion beam was turned off for 90 seconds to prevent excess heat buildup on the surface. Milling was then resumed for an additional 90 seconds. Sample S#2 followed the same protocol but with higher ion beam currents of 17 mA for the first 90 s and 18 mA for the second 90 s period.

Once the ion milling process was complete, we immediately transferred the milled GaAs (111) substrate to a vacuum chamber ('prep' chamber, connected to the MBE system) with a base pressure of 5×10^{-9} Torr to minimize exposure to air. We observed that if the milled substrate was exposed to air for more than 15 minutes, it resulted in films with poor crystalline quality with high surface roughness or even polycrystalline films, likely due to the substrate's high sensitivity to oxidation. To mitigate this, the next step involved degassing the substrate in vacuum at 220°C for 45 minutes to 1 hour in vacuum, which helps remove contaminants such as water, hydrocarbons, and oxygen, creating a clean surface. Following degassing, the substrate was transferred in vacuum to the MBE chamber (base pressure $< 5 \times 10^{-10}$ Torr) and annealed at 600°C for 5-6 minutes to eliminate any remaining organic residues, smoothen the surface, and promote the desired surface reconstruction. This process is believed to enhance nucleation and adhesion, leading to high-quality thin films with improved properties. During the annealing, we monitored the reflection

high-energy electron diffraction (RHEED) pattern of the substrate using a 10 kV acceleration voltage for the electrons. For S#2, we observed the first signs of RHEED streaks around 500°C, with the majority of streaks becoming visible at 550°C. At 600°C, after maintaining the temperature for 5-6 minutes, half-order streaks were observed, consistent with a 2 x 2 surface reconstruction (see Fig. 1). However, for S#1, no RHEED streaks were detected up to 550°C. Upon reaching 600°C, only the integer order streaks appeared after a 5-7 minute wait, as shown in Fig. 1(a), with no visible half-order features. Further annealing at 600°C led to a decrease in the intensity of these streaks, and increasing the annealing temperature did not result in any improvement.

After annealing, the substrate is cooled down rapidly to room temperature by shutting power to the substrate heater. The substrate was typically allowed to cool further overnight with the manipulator held at 19°C. Bi films are then deposited in a typical base pressure $< 1.5 \times 10^{-10}$ Torr in the chamber. The deposition rate, monitored by a quartz crystal microbalance (QCM), was approximately 0.013 Å/sec for all films in this study.

The RHEED pattern during Bi (111) film growth is shown in Figure 1. For S#1, 3D spotty RHEED patches were observed for the first 5-8 nm of deposition (Fig. 1(b)), indicating island-like growth. These islands are supposed to be Bi (110)¹² as we have also observed in x-ray scans of films in this range. As the deposition continues and the thickness increases, these islands coalesce, eventually leading to the growth of an epitaxial Bi (111) film, where the peaks corresponding to the (110) oriented phase are no longer visible in x-ray diffraction. After the deposition of 24 nm Bi, the RHEED intensity was weak as shown in Fig. 1c, requiring a higher emission current (-2.1 μA) for better visibility as shown in Fig. 1(d), indicating a relatively poor surface quality of the Bi

film. In contrast, S#2 exhibits clear 2D RHEED streak patterns at a much lower Bi thickness of around 5 nm, even with significantly lower emission current (-0.6 μ A). As the Bi deposition continues, the intensity of the streaky RHEED pattern increases, and by 24 nm of film growth sharp 2D diffraction spots are observed indicating nearly atomically smooth crystalline surfaces (Fig. 1(f-h)). Further examination of the surface quality was conducted using atomic force microscopy (AFM) images, shown in Fig. 2. The triangular patterns in the AFM images confirmed the Bi (111) with trigonal axis is perpendicular to the film surface. Notably, in S#1, the domains were randomly oriented (Fig. 2b), while in S#2, the domains predominantly follow a preferential direction (Fig. 2c), which can be interpreted as a local absence of rotational twin domains^{24,37}.

X-ray diffraction (XRD) measurements of the two films are carried out on a Bruker D8 system and the results are presented in Fig. 2d . The (111) peaks at 22.354° and 22.440°, as well as the (222) peaks at 45.645° and 45.752° in 2theta-scan for S#2 and S#1, and notably the (110) peaks are absent, consistent with a highly crystalline single-phase Bi (111) film. These peak positions differ slightly from the bulk Bi sample values of 22.491° and 45.888°, suggesting some deviations in the film's lattice structure possibly due to the lattice mismatch between the substrate and the film. For S#1, the rocking curve for the (111) peak has a full width at half maximum (FWHM) of 0.157°, which is nearly double that for S#2 of 0.098°, indicating a larger mosaic spread in S#1 compared to S#2, as shown in Fig. 2(d). This difference highlights the variation of crystalline quality with substrate preparation.

To further investigate the epitaxial relationship between the GaAs substrate and Bi films, we performed X-ray reflectivity (XRR) and phi-scan XRD measurements on the Bi (121) and (221) peaks ((01 $\bar{1}$ 4) and (10 $\bar{1}$ 5) in hexagonal indices) and (220) peak of the GaAs substrate, as shown

in Fig. 2e and 2f. The oscillations in the XRR curves of S#1 damped more rapidly than that of S#2, despite both having nearly the same thickness (see Supplementary Materials Fig. S1). This suggests that the surface and/or interface of S#1 is relatively rough compared to S#2. The in-plane phi-scan of the Bi (121) peak reveals a total of twelve peaks, with six strong peaks and six weaker peaks. For S#2, the intensity of the weaker peaks $\sim 10^{-2}$ of the stronger peak, while for S#1 this ratio is 10^{-1} , suggesting the presence of four sets of twin planes. Notably, the GaAs peaks are offset by $\sim 30^\circ$ in φ from peaks corresponding to the majority Bi (111) domains and are thus at approximately the same azimuthal orientation (within 0.3°) as the minority Bi domains. Additionally, the intensity of the Bi peaks in S#2 is approximately 1.5 times stronger than in S#1, signifying a better in-plane domain alignment in S#2 compared to S#1.

The Bi (111) films were lithographically patterned into six-probe Hall bar devices for magneto-transport measurements. We first discuss our results from four samples, S#1 and S#2 with thickness 24 nm, and also two other films of thickness 16 nm and 32 nm both prepared under conditions identical to S#2. The Hall bar device width was 200 μm , and the distance between the voltage tabs was approximately 700 μm (Fig. 3(a)), and the distance between the current leads was approximately 2 mm. Pt/Au contact pads were deposited for wire bonding to the leads. The magnetic field was applied perpendicular to the film plane for all measurements. The longitudinal resistance and transverse Hall signals were measured by sweeping the magnetic field from +14 T to -14 T, and to eliminate the effect of the magnetic field on the longitudinal component of the resistivity contributing to the measured Hall voltage, we anti-symmetrized the Hall signal.

Shown in Fig. 3(d) is the change in sheet resistance with decreasing temperature for S#1 and S#2 samples. The increase in resistance with decreasing temperature for both the samples suggests a

transition from semi-metallic to semiconductor-like behavior, driven by the bulk of the thin film becoming insulating while the surface remains predominantly conducting. This contrasts with bulk Bi crystals, which exhibit metallic behavior with resistivity decreasing with decreasing temperature^{20,36,37}. It is worth noting that the resistance in S#1 is higher compared to S#2. Fig. 3(b, c) and 3(e, f) showed the longitudinal magnetoresistance (MR) and transverse conductivity for S#1 and S#2 at different temperatures. The MR is defined as:

$$MR = \frac{\rho_{xx}(B) - \rho_{xx}(0)}{\rho_{xx}(0)} \quad \text{Eq. 1}$$

where $\rho_{xx}(B)$ and $\rho_{xx}(0)$ are the resistivity with and without magnetic field B applied perpendicular to the film plane at a given temperature. The longitudinal resistivity is defined as $\rho_{xx} = R_{xx}W \cdot t / L$, where W (200 μm) and L (700 μm) are the width and length of the Hall bar, respectively, and t is the thickness of the Bi films, and ρ_{xy} ($= R_{xy} \cdot t$) is the transverse resistivity, and this allows us to calculate $\sigma_{xy}(B) = \frac{-\rho_{xy}}{\rho_{xy}^2 + \rho_{xx}^2}$ and $\sigma_{xx} = \frac{\rho_{xx}}{\rho_{xy}^2 + \rho_{xx}^2}$ as a function of B for our films.

The transport measurements shown in Fig. 3(g) and Fig. 3(j), reveal that the sheet resistance of the 16 nm Bi film is more than twice that of the 32 nm Bi film. The 32 nm film exhibited very large MR of around 112% while the 16 nm film showed significantly lower values of 35%, suggesting that thinner films have notably reduced mobility. In bulk Bi crystals, magnetoresistance (MR) typically exhibits its highest values at low temperatures³⁸⁻⁴⁰ and gradually decreases with increasing temperature. In contrast, Bi thin films in this study display an opposite trend, where MR increases with temperature and reaches a maximum around 200 K for all samples (see Fig. 3). At room temperature, MR becomes nearly linear, with a slightly reduced value compared to the peak

at 200 K. For the 16 nm, 24 nm (S#2), and 32 nm films, at low temperatures (5K) the MR rises sharply at low magnetic fields and then more gradually at higher fields.

It is worth noting a few key differences in the magneto-transport of samples S#1 and S#2, (both 24 nm thick). In S#2, there is a relatively sharp rise in MR up to approximately ± 4 T, followed by a gradual increase, reaching 18.7% at ± 14 T. In contrast, MR in S#1 shows a weaker response to the magnetic field, with its value peaking up to 8.35% at ± 14 T (Fig. 3(c)). We attribute this to higher scattering rates in S#1, as evident from lower MR and higher values of resistance vs temperature, suggests that it has lower mobilities compared to S#2. We also plot the transverse conductivity (σ_{xy}) of both samples, as shown in Fig. 3(c) and 3(f). The σ_{xy} of S#2 at 5 K exhibited a highly nonlinear inverted S-shaped curve with negative slope at low fields and a sharp min/max at ± 1.3 T. As we shall see below, the negative slope at lower fields (from 0T to 1.3T) and the inverted S-shape observed in S#2 originates from high mobility electrons, as observed in bulk single-crystals of other high-mobility semimetals⁴¹⁻⁴⁴. Beyond these extrema, σ_{xy} decreases in magnitude eventually crossing zero and changing sign at 9.6 T. On increasing the field further, σ_{xy} increases linearly in magnitude with a positive slope up to 14 T. This is due to the presence of a relatively low mobility hole pocket coexisting with the high-mobility electrons. In contrast, sample S#1 at 5 K showed a much weaker high mobility electron pocket feature in the low-field region, and σ_{xy} has a positive slope with magnetic field over the entire range, indicating a dominant hole-type carrier.

As noted earlier, for films in the thickness range presented here, the bulk states of Bi are gapped out and the density of states at the Fermi level is dominated by strongly spin-split Bi (111) surface states, with an electron pocket at Γ , hole pockets (6) between Γ and M and electron pockets (6)

near the M -point. We denote their carrier densities by n_e^{Γ} , n_h , and n_e^M , and their carrier mobilities by μ_e^{Γ} , μ_h , μ_e^M . A multi-band model for the conductivity of these surface states would be given by⁴⁵:

$$\sigma_{xx}(B) = \sum_i \frac{en_i\mu_i}{1+(\mu_i B)^2} \quad \text{Eq. 2a}$$

$$\sigma_{xy}(B) = eB \sum_i \frac{sen_i\mu_i^2}{1+(\mu_i B)^2} \quad \text{Eq. 2b}$$

where $s = +/-$ for electrons/holes. We fit the expressions for σ_{xy} and σ_{xx} in Eq. 2 simultaneously to the measured data to solve for the densities/mobilities of the different pockets. We tried a three-band model (3BM) with two electron pockets and one hole pocket, and a two-band model (2BM) with one electron pocket and one hole pocket.

In our fits to the 16 nm, 24 nm (S#2) and 32 nm samples, we found that σ_{xy} and σ_{xx} were dominated by a single high-mobility electron pocket (this signature was much less prominent in sample S#1). This electron pocket has a high enough mobility such that the measured σ_{xy} from these samples have prominent maxima/minima at all temperatures at $B < 5$ T, which should occur when the condition $|\mu_e B| \sim 1$ is met, according to Eq. 2b. The slope of the Hall conductivity near zero field $\frac{d\sigma_{xy}}{dB} |_{B=0} = \sum_i sen_i \mu_i^2$ ($s = +/-$ for electrons/holes) is also dominated by the same high-mobility electron-like pocket. This places strong constraints on the values of n_e and μ_e for the high-mobility pocket extracted from multi-band fits to the data. Specifically, using a 3BM to fit to the data for sample S#2 (24 nm) at 5 K, we find $\mu_e = 6137 \text{ cm}^2 \text{V}^{-1} \text{s}^{-1}$ and $n_e = 6.48 \times 10^{11} \text{ cm}^{-2}$ for this high-mobility electron pocket, while for a 2BM we find $\mu_e = 5847 \text{ cm}^2 \text{V}^{-1} \text{s}^{-1}$ and $n_e = 8.03 \times 10^{11} \text{ cm}^{-2}$. Since the 3BM yields a better fit to the data (Fig. 4 (a,b), Fig. S2 (b-d)), we use

the fit parameters from the 3BM to describe our samples. As we will discuss below, these high mobility electrons are most likely from the electron pocket near the M -point. We note that if the remaining electron and hole pockets have relatively low mobility ($\mu_i B \ll 1$), then according to Eq. 2b, each should make a quasi-linear contribution to the Hall conductivity i.e. $\sigma'_{xy}(B) \sim \sum_i s n_i \mu_i^2 B$. Each low-mobility pocket should also make a contribution to longitudinal conductivity, with a quadratic dependence on field, $\sigma'_{xx}(B) \sim \sum_i e n_i \mu_i (1 - \mu_i^2 B^2) = \sum_i \sigma_{xx_i}(0) (1 - \mu_i^2 B^2)$. Indeed, if we calculate the contributions to conductivity from the high mobility electrons using (n_e, μ_e) from our 3BM fit (see Fig. 4 (c,d) for example), and subtract this from our conductivity data, the remainder (σ') is consistent with this hypothesis. This leaves us with three constraints for σ' : $\frac{d\sigma'_{xy}}{dB}|_{B=0}$, $\sigma'_{xx}(0)$, and $\sum_i \sigma_{xx_i}(0) \mu_i^2$, the coefficient of the quadratic term in $\sigma'_{xx}(B)$. However, for the two lower mobility bands in a 3-band model, we have four parameters – two (n_i, μ_i) for each band, and the fit is under-constrained, and the extracted values have limited usefulness⁴⁶. Correspondingly, for the 2-band model with only one low mobility pocket, the fit is over-constrained, and the fits are inadequate. A third pocket is needed to fit to the magnitude of the total longitudinal conductivity at zero field and the magnetoconductance. Thus, while we obtain better fits using a 3-band vs a 2-band model, we cannot determine (n_i, μ_i) uniquely for the two low-mobility bands in the 3-band model, and we do not present these values here. From our 3BM fit for sample S#1 we find a lower mobility for the ‘high-mobility’ electron pocket, with $\mu_e = 2942 \text{ cm}^2 \text{V}^{-1} \text{s}^{-1}$, though the fits to the data using the 3-band model are not as discerning because the high-mobility ‘inverted-S’ feature is much weaker.

We note that for all samples, n_e increases with increasing temperature (Fig. 4f). This suggests that the very low carrier density in the high-mobility electron pocket that dominates σ_{xy} at low fields

can change significantly due to thermal activation of carriers across a small gap. Thermal excitation leads to higher carrier densities, particularly for electrons in the high mobility pocket, resulting in higher conductivity. This is observed even in the relatively low-mobility S#1, where a pronounced ‘inverted-S’ shape emerges in σ_{xy} at higher temperatures at low fields, accompanied by higher magnetoresistance (Fig.3 (b,c)). Table 1 summarizes the mobilities and carrier concentrations of all the films studied.

In order to understand the origin of the high mobility electrons in our thin film samples, we consider the limit where the bulk states are gapped out at the lowest temperatures, and the conductivity is dominated by the surface states. We take $\mathbf{k}\cdot\mathbf{p}$ models for the electron pocket at Γ ⁴⁷, hole pockets between Γ and M ⁴⁸, and the electron pockets near the M -point⁴⁹ to $O(k^2)$ and compute the Hall conductivity due to the orbital field for each pocket, fitting parameters from the $\mathbf{k}\cdot\mathbf{p}$ model to a tight-binding model^{49,50}. The Hall conductivity for each pocket is given by:

$$\sigma_{xy} = \frac{e^2}{4\pi} (m^* v_{Fx} v_{Fy}) \tau \frac{\Omega\tau}{1+(\Omega\tau)^2} \quad \text{Eq. 3}$$

where e is the electronic charge, m^* is the effective mass of the pocket, v_{Fx} and v_{Fy} are the Fermi velocities in the x and y direction – the major and minor axes of the ellipsoid that we use to model the Fermi surfaces for these pockets. (we note for the e -pocket near Γ , $v_{Fx} = v_{Fy}$ to $O(k^2)$). We use the relaxation time approximation, where τ is the elastic relaxation time for all electron and hole pockets, and $\Omega = eB/m^*$ is the cyclotron frequency for each pocket. Using the fitted parameters from the tight binding model, we compare the quantity $\tilde{\sigma}_{xy} = m^* v_{Fx} v_{Fy}$ for each set of pockets, taking note that there is one electron pocket centered at Γ , 6 hole pockets between Γ and M , and 6 electron pockets near the M -points of the Brillouin zone. Using units $\hbar = 1$, we arrive at

$\tilde{\sigma}_{xy,e-M} = 0.28eV$; $\tilde{\sigma}_{xy,h} = .08eV$; $\tilde{\sigma}_{xy,e-\Gamma} = 0.11eV$. We thus see that the contribution from the electron pockets near the M -point dominate the Hall conductivity, due in large part to the electron pockets away from Γ having the largest effective mass, $m_{el}^{M*} > m_h^* > m_{el}^{\Gamma*}$. Thus, our hypothesis is that in films where the thickness $\geq 16\text{nm}$, the high mobility electrons that give rise to the characteristic ‘S’-shaped Hall conductivity originate in the electron pockets in the Bi (111) surface state in vicinity of the M -point, with (n_e^M, μ_e^M) .

Through our optimized substrate treatment and annealing conditions, we also grew epitaxial Bi (111) films down to thickness of approximately 5 nm. These films exhibit excellent stability in ambient conditions without oxidation, which enabled us to perform various ex-situ measurements, including atomic force microscopy and x-ray diffraction and reflectivity, and transport measurements on patterned devices (Fig. 5). AFM analysis revealed a smooth surface with an estimated root mean square (RMS) roughness of 0.41 nm. The (121) phi scan showed peaks at similar positions to those observed in thicker films, albeit with significantly weaker intensities. Additionally, resistivity measurements indicated an increase with decreasing temperature, suggesting an insulating behavior in this ultra-thin film. Interestingly, similar resistivity trends have been observed in ultra-thin bismuth layers (~ 0.39 nm) grown between a 6H-SiC substrate and epitaxial graphene via confinement heteroepitaxy²⁵. Furthermore, we note an increase in resistance upon cooling to the lowest temperatures, starting at around 4.5 K. This behavior, also observed in thin films of topological materials⁵¹, could be due to electron-electron interactions. Importantly, Hall measurements revealed sublinear hole-like R_{xy} vs B curves, at low temperatures (Fig. 5d). As the temperature increases, hole-like carriers continue to dominate at higher temperatures (Fig. S4 (a)), in contrast to the S#1 sample, which exhibited inverted S-shaped curves due to the presence of both holes and high-mobility electrons at higher temperatures. This suggests

that in the ultra-thin 5 nm Bi film, the Hall signal is dominated by hole-like carriers, and the high mobility electron pocket is gapped out to the extent that it does not get populated even at higher temperatures. It is known from ARPES measurements¹⁸ and from theoretical calculations²⁷ that the high-mobility electron pockets in the Bi (111) surface near the *M*-point are strongly hybridized with the gapped Dirac like bulk states. Confinement effects push the bulk electron-like states near the *M*-point further above the Fermi level¹⁸, pulling the surface state electron pockets near the *M*-point with them, causing them to get depopulated. Consequently, the transport properties become dominated by the relatively low mobility hole pockets with (n, μ_h) that lie along the Γ -*M* direction, as observed in the 5 nm Bi film. We also observed a cusp-like behavior, characteristic of the weak antilocalization (WAL) effect, in the low-field region near zero in our longitudinal resistance. This effect is typically observed at low temperatures in thin films of two-dimensional systems with strong spin-orbit coupling (SOC), due to weak anti-localization⁵². Similar cusp-like behavior is also present in other thicker samples but is less pronounced in the 24 nm (S#2) and 32 nm films and tends to vanish with increasing temperatures (see Fig. S4(b)).

In conclusion, for ultrathin epitaxial Bi films grown on GaAs (111) substrates, we found that argon ion milling, annealing, and growth conditions significantly affect film growth and electrical transport properties. For films grown on substrates prepared under conditions where the 2 x 2 reconstruction was not as evident, the films showed lower mobilities. In contrast, films on substrates with optimized milling and annealing conditions where the 2 x 2 reconstruction was evident exhibit smoother surfaces, larger unidirectional domains, higher conductivity, and larger positive MR in perpendicular fields at low temperatures. Our theoretical models indicated that these high-mobility electrons originate in the electron pocket near the *M*-point in the spin-split surface states of Bi (111). Our findings provide a clear procedure for growing high-quality large

area Bi thin films on GaAs (111) substrates, where the electronic properties can be tuned by varying the thickness. These films may have potential applications in spintronics and in fundamental studies of the spin textured surface states of Bi (111).

Acknowledgements: The synthesis and characterization of samples presented in this study, and their phenomenological modeling was supported by the Center for the Advancement of Topological Semimetals (CATS), an Energy Frontier Research Center funded by the U.S. Department of Energy (DOE) Office of Science (SC), Office of Basic Energy Sciences (BES), through the Ames National Laboratory under contract DE-AC02-07CH11358. The calculations of the surface-state electronic structure in Bi thin films were carried out by S. Ambhire and S. S.-L. Zhang, with support from the College of Arts and Sciences at CWRU. The $\mathbf{k}\cdot\mathbf{p}$ model was worked out by M.D.S. and I.M. E.D.A., J.S.W., J.S.J. and J.Y. assisted in this research and were supported by the Materials Science and Engineering Division, Office of Basic Energy Sciences, U.S. Department of Energy. Work performed at the Center for Nanoscale Materials, a U.S. Department of Energy Office of Science User Facility, was supported by the U.S. DOE, Office of Basic Energy Sciences, under Contract No. DE-AC02-06CH11357.

Data Availability Statement: All data presented in this paper will be available via the Harvard Dataverse upon publication.

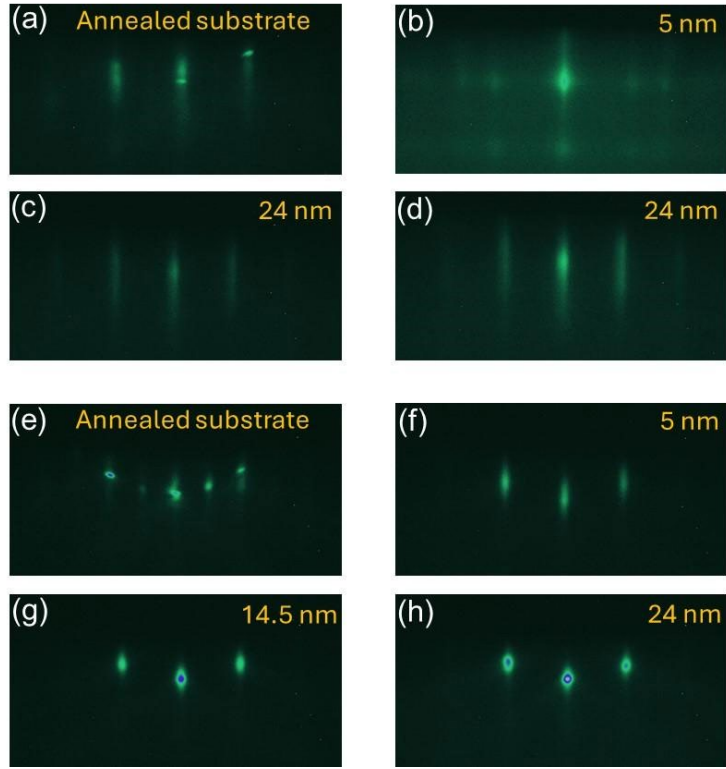


Figure 1: (a) RHEED pattern of the GaAs (111) substrate for S#1 taken along the $(11\bar{2})$ azimuth after annealing. Prior to annealing, the substrate was ion milled with an Ar^+ ion beam current of 16 mA. The ion milling process was performed twice, each time for 90 s with a 90 s gap between the milling sessions. (b) A 3D spotty RHEED pattern indicating island growth of Bi in the initial stages of growth. (c, d) RHEED patterns of the 26 nm epitaxial Bi film at emission currents of $-0.9 \mu\text{A}$ and $-2.1 \mu\text{A}$, respectively. (e) RHEED pattern of the GaAs (111) substrate for S#2 taken along the $(11\bar{2})$ azimuth after annealing, showing evidence for a 2×2 reconstruction. Prior to annealing, the substrate was ion milled with ion beam currents of 17 mA and 18 mA for 90 s each, with a 90 s gap between the milling sessions. (f-h) In this case, epitaxial Bi film started to grow in an atomic layer-by-layer manner from an earlier stage, showing 2D RHEED patterns. The RHEED images were captured at different Bi deposition thicknesses at a lower emission current of $-0.6 \mu\text{A}$.

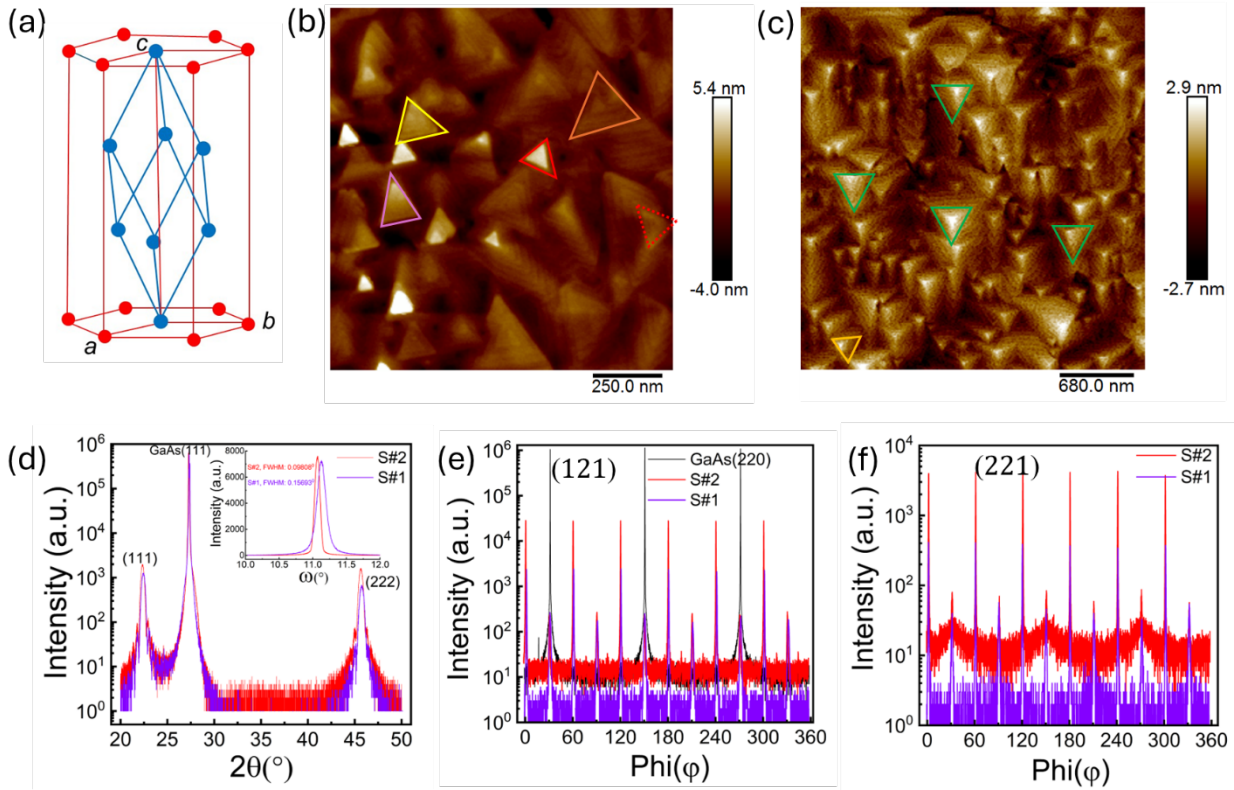


Figure 2: (a) Schematic diagram of rhombohedral Bi lattice (blue lines) in a hexagonal lattice (red lines). Not all atoms are shown in the schematic. (b) AFM image of sample S#1. (c) AFM image of sample S#2. Different triangular domains are marked with different colors. (d) Both Bi films peaks are denoted by (111) and (222) peaks of both the samples in the 2theta-theta XRD measurements. (e, f) Phi-scan of the tilted (121) and (221) ((01₁4) and (10₁5) in hexagonal indices) planes of S#1(purple) and S#2 (red) samples. The (220) plane of the GaAs substrate shows the three-fold symmetry (black). The weaker intensity observed for the (221) plane of Bi compared to the (121) plane is primarily attributed to a smaller structure factor, which reduces the diffracted intensity despite similar measurement geometry.

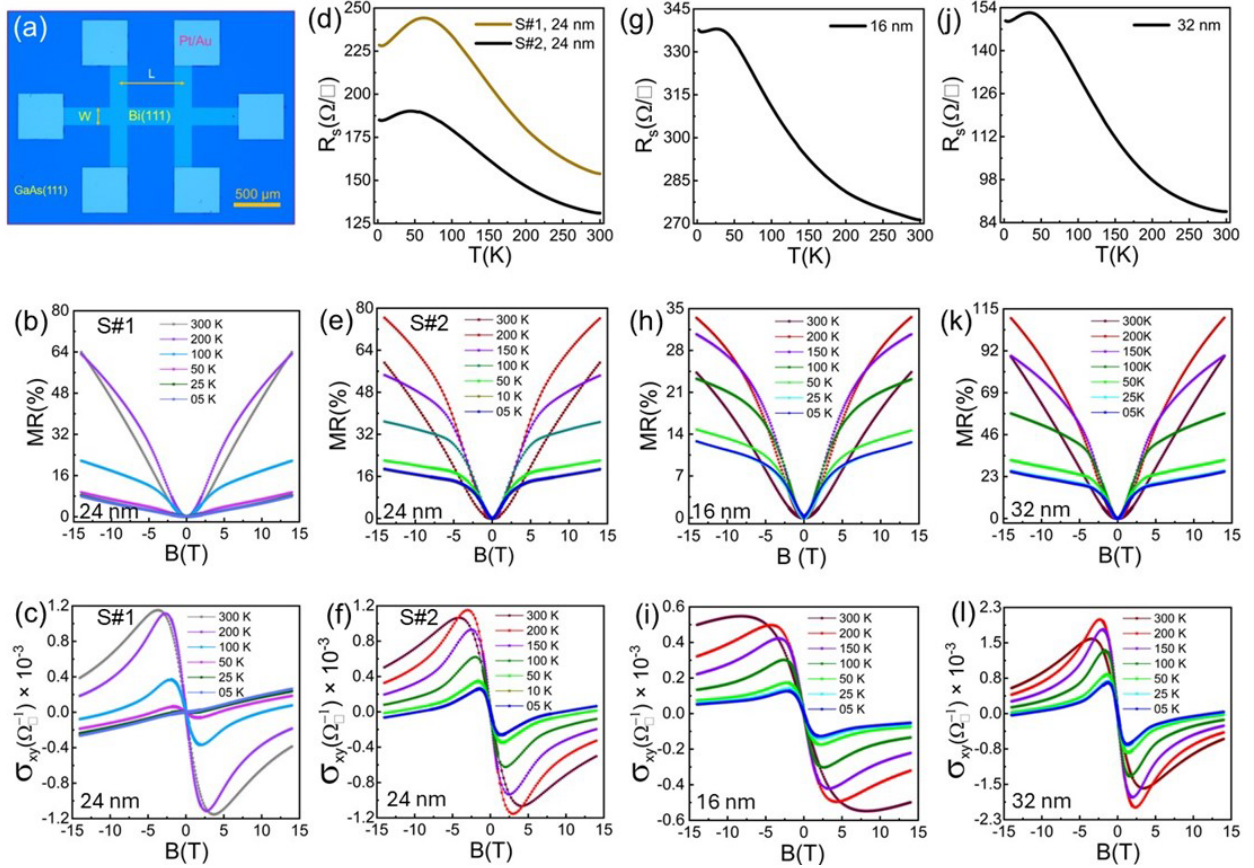


Figure 3: (a) Lithographically patterned Hall bar device. W and L represent the width and length of the Hall bar, respectively. The scale bar corresponds to 500 μm . (b, c) magnetoresistance and Hall conductivity of S#1 at different temperatures. Note, S#1 was the only sample grown on a GaAs (111) substrate that did not show the 2×2 reconstruction. (d) Sheet resistance vs temperature curves for S#1 and S#2 samples, both 24 nm thick. (e, f) Hall conductivity and magnetoresistance of S#2 at different temperatures. (g, h, i) Sheet resistance vs field at different temperatures for a 16 nm Bi film. (j, k, l) Sheet resistance, magnetoresistance and Hall conductivity with field at different temperatures for a 32 nm Bi film.

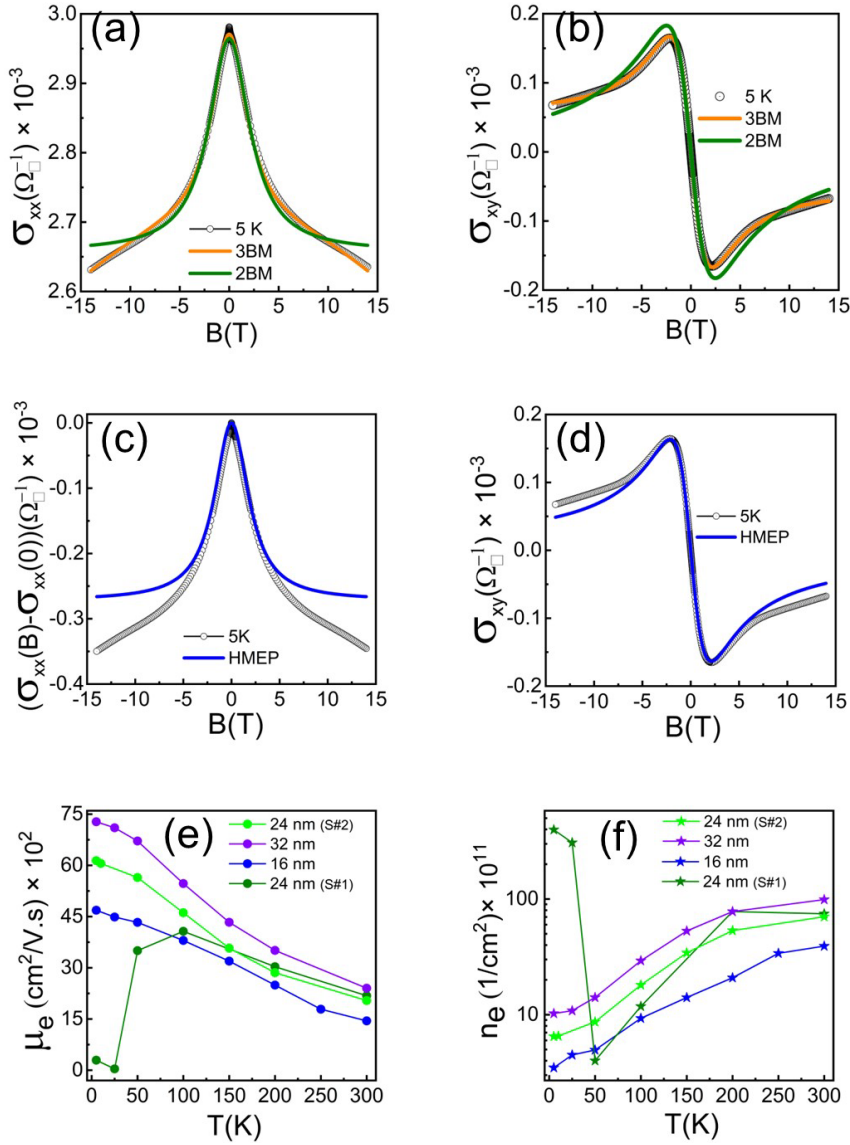


Figure 4 (a) Longitudinal conductivity $\sigma_{xx}(B)$ and (b) Hall conductivity $\sigma_{xy}(B)$ at 5 K for a 16 nm Bi (111) film deposited on a substrate where the 2 x 2 reconstruction was clearly evident. Fitting to a 3-band model was shown to work better than to a 2-band model, and both show evidence for an electron pocket with high mobility. (c) Comparison of the contribution from the high-mobility electron pocket (HMEP) to the change in longitudinal conductivity with field, and (d) the Hall conductivity, using mobility and carrier density obtained from a 3-band model fit. (e,f) Mobility and areal carrier density of electrons in the high mobility pocket as a function of temperature, extracted from fitting a three-band model to $\sigma_{xx}(B)$ and $\sigma_{xy}(B)$.

Thickness (nm)	μ_e (5 K) cm ² /V-s	n_e (5 K) cm ⁻²	μ_e (300 K) cm ² /V-s	n_e (300 K) cm ⁻²
16 nm	4686	3.48×10^{11}	1445	3.91×10^{12}
24(#S1)	0294	3.97×10^{13}	2182	7.46×10^{12}
24(#S2)	6137	6.48×10^{11}	2039	7.03×10^{12}
32	7277	1.02×10^{12}	2402	9.88×10^{12}

Table 1 Properties of the high mobility electron pocket extracted from simultaneous fits to $\sigma_{xx}(B)$ and $\sigma_{xy}(B)$ at 5 K and at 300 K for different thicknesses.

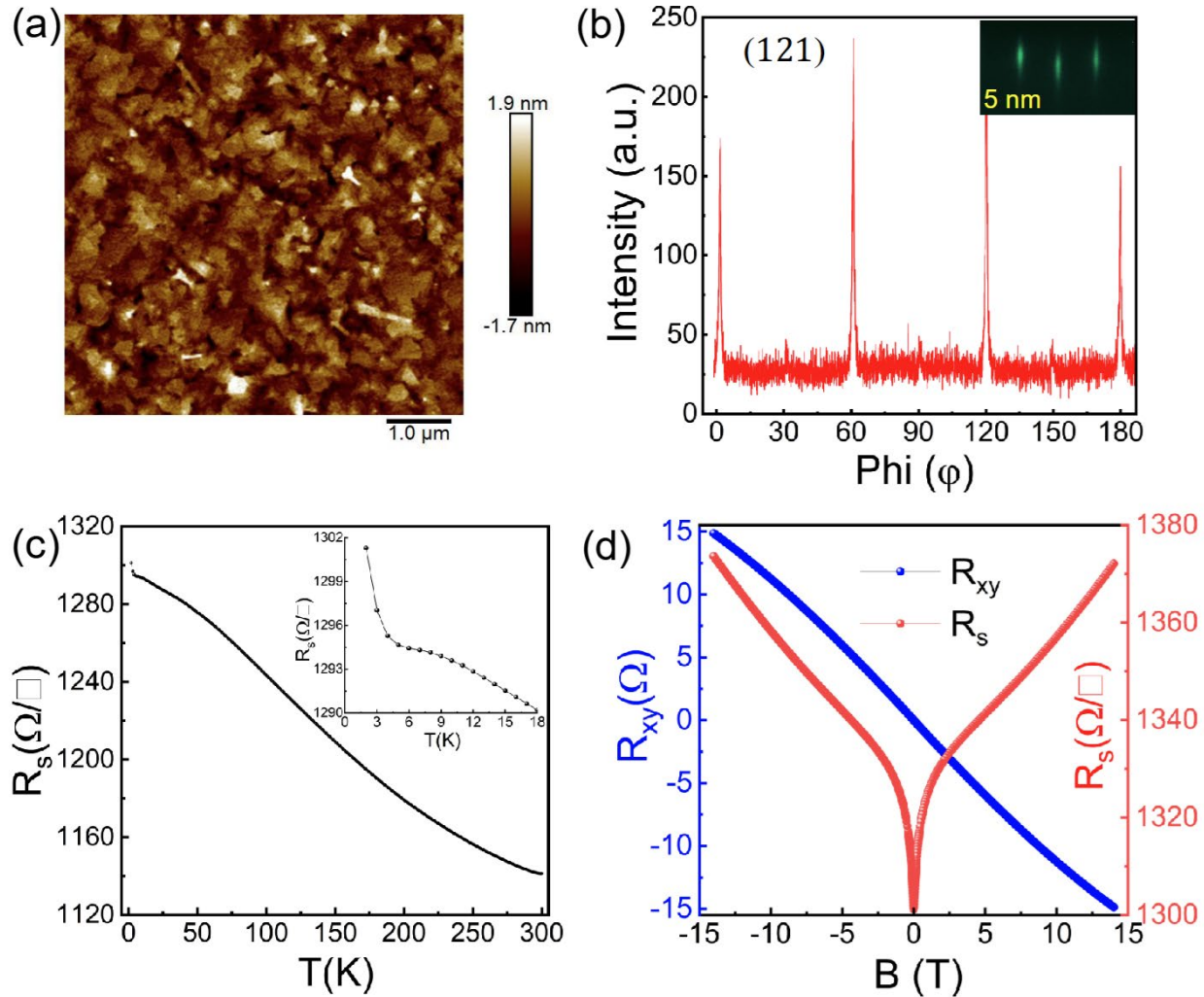


Figure 5: (a) Atomic force microscopy image of a 5 nm thick Bi film. (b) Azimuthal (phi) scan of the Bi (121) peak in a 5 nm thick film. The inset shows the RHEED pattern after film growth. (c) Sheet resistance vs temperature curves from 300 K down to 2 K. The sharp rise of resistance from 4.5 K is shown in the inset. (d) Sheet resistance R_s (red) and hall resistance R_{xy} (blue) vs. magnetic field at 2 K.

References

- 1 V. S. Edelman, "Electrons in Bismuth," *Advances in Physics* **25**, 555-613 (1976). <https://doi.org/10.1080/00018737600101452>
- 2 P. Hofmann, "The surfaces of bismuth: Structural and electronic properties," *Progress in Surface Science* **81**, 191-245 (2006). <https://doi.org/10.1016/j.progsurf.2006.03.001>
- 3 CA Hoffman, JR Meyer, FJ Bartoli, A Di Venere, XJ Yi, CL Hou, HC Wang, JB Ketterson, and GK Wong, "Semimetal-to-semiconductor transition in bismuth thin films," *Physical Review B* **48**, 11431 (1993). <https://doi.org/10.1103/PhysRevB.48.11431>
- 4 F Reis, G Li, L Dudy, M Bauernfeind, S Glass, W Hanke, R Thomale, J Schäfer, and R Claessen, "Bismuthene on a SiC substrate: A candidate for a high-temperature quantum spin Hall material," *Science* **357**, 287-290 (2017). <https://doi.org/10.1126/science.aai8142>
- 5 Jian Gou, Hua Bai, Xuanlin Zhang, Yu Li Huang, Sisheng Duan, A Ariando, Shengyuan A Yang, Lan Chen, Yunhao Lu, and Andrew Thye Shen Wee, "Two-dimensional ferroelectricity in a single-element bismuth monolayer," *Nature* **617**, 67-72 (2023). <https://doi.org/10.1038/s41586-023-05848-5>
- 6 Ilya K Drozdov, Aris Alexandradinata, Sangjun Jeon, Stevan Nadj-Perge, Huiwen Ji, RJ Cava, B Andrei Bernevig, and Ali Yazdani, "One-dimensional topological edge states of bismuth bilayers," *Nature Physics* **10**, 664-669 (2014). <https://doi.org/10.1038/nphys3048>
- 7 M. Jankowski, D. Kaminski, K. Vergeer, M. Mirolo, F. Carla, G. Rijnders, and T. R. J. Bollmann, "Controlling the growth of Bi(110) and Bi(111) films on an insulating substrate," *Nanotechnology* **28** (2017). <https://doi.org/10.1088/1361-6528/aa61dd>
- 8 Yunhao Lu, Wentao Xu, Mingang Zeng, Guanggeng Yao, Lei Shen, Ming Yang, Ziyu Luo, Feng Pan, Ke Wu, and Tanmoy Das, "Topological properties determined by atomic buckling in self-assembled ultrathin Bi (110)," *Nano Letters* **15**, 80-87 (2015). <https://doi.org/10.1021/nl502997v>
- 9 Hadass S. Inbar, Muhammad Zubair, Jason T. Dong, Aaron N. Engel, Connor P. Dempsey, Yu Hao Chang, Shinichi Nishihaya, Shoaib Khalid, Alexei V. Fedorov, Anderson Janotti, and Chris J. Palmstrøm, "Structural inversion asymmetry in epitaxial ultrathin films of Bi(111)/InSb(111)B," *Physical Review Materials* **9**, 054202 (2025). <https://doi.org/10.1103/PhysRevMaterials.9.054202>
- 10 Nan Wang, Y-X Dai, T-L Wang, H-Z Yang, and Yang Qi, "Investigation of growth characteristics and semimetal–semiconductor transition of polycrystalline bismuth thin films," *IUCrJ* **7**, 49-57 (2020). <https://doi.org/10.1107/S2052252519015458>
- 11 Zijian Jiang, Victoria Soghomonian, and Jean J Heremans, "Carrier properties of Bi (111) grown on mica and Si (111)," *Physical Review Materials* **6**, 095003 (2022). <https://doi.org/10.1103/PhysRevMaterials.6.095003>
- 12 Shinichiro Hatta, Yoshiyuki Ohtsubo, Sanae Miyamoto, Hiroshi Okuyama, and Tetsuya Aruga, "Epitaxial growth of Bi thin films on Ge (1 1 1)," *Applied Surface Science* **256**, 1252-1256 (2009). <https://doi.org/10.1016/j.apsusc.2009.05.079>

13 Martin Kammler and Michael Horn-von Hoegen, "Low energy electron diffraction of epitaxial growth of bismuth on Si (1 1 1)," *Surface Science* **576**, 56-60 (2005).
<https://doi.org/10.1016/j.susc.2004.11.033>

14 Ikuya Kokubo, Yusaku Yoshiike, Kan Nakatsuji, and Hiroyuki Hirayama, "Ultrathin Bi (110) films on Si (111) 3× 3-B substrates," *Physical Review B* **91**, 075429 (2015).
<https://doi.org/10.1103/PhysRevB.91.075429>

15 C. R. Ast and H. Höchst, "Fermi surface of Bi(111) measured by photoemission spectroscopy :- art. no. 177602," *Physical Review Letters* **87** (2001).
<https://doi.org/10.1103/PhysRevLett.87.177602>

16 T. Hirahara, K. Miyamoto, A. Kimura, Y. Niinuma, G. Bihlmayer, E. V. Chulkov, T. Nagao, I. Matsuda, S. Qiao, K. Shimada, H. Namatame, M. Taniguchi, and S. Hasegawa, "Origin of the surface-state band-splitting in ultrathin Bi films: from a Rashba effect to a parity effect," *New Journal of Physics* **10** (2008). <https://doi.org/10.1088/1367-2630/10/8/083038>

17 T. Hirahara, T. Nagao, I. Matsuda, G. Bihlmayer, E. V. Chulkov, Y. M. Koroteev, P. M. Echenique, M. Saito, and S. Hasegawa, "Role of spin-orbit coupling and hybridization effects in the electronic structure of ultrathin Bi films," *Physical Review Letters* **97** (2006).
<https://doi.org/10.1103/PhysRevLett.97.146803>

18 S. Ito, M. Arita, J. Haruyama, B. Feng, W. C. Chen, H. Namatame, M. Taniguchi, C. M. Cheng, G. Bian, S. J. Tang, T. C. Chiang, O. Sugino, F. Komori, and I. Matsuda, "Surface-state Coulomb repulsion accelerates a metal-insulator transition in topological semimetal nanofilms," *Science Advances* **6** (2020). <https://doi.org/10.1126/sciadv.aaz5015>

19 S. Ito, B. Feng, M. Arita, A. Takayama, R. Y. Liu, T. Someya, W. C. Chen, T. Iimori, H. Namatame, M. Taniguchi, C. M. Cheng, S. J. Tang, F. Komori, K. Kobayashi, T. C. Chiang, and I. Matsuda, "Proving Nontrivial Topology of Pure Bismuth by Quantum Confinement," *Physical Review Letters* **117** (2016). <https://doi.org/10.1103/PhysRevLett.117.236402>

20 VN Lutskii, "Features of optical absorption of metallic films in the region where the metal turns into a dielectric," *ZhETF Pisma Redaktsiiu* **2**, 391 (1965).

21 Y. Ohtsubo, L. Perfetti, M. O. Goerbig, P. Le Fèvre, F. Bertran, and A. Taleb-Ibrahimi, "Non-trivial surface-band dispersion on Bi(111)," *New Journal of Physics* **15** (2013).
<https://doi.org/10.1088/1367-2630/15/3/033041>

22 M. A. Ortigoza and T. S. Rahman, "A closer look at how symmetry constraints and the spin-orbit coupling shape the electronic structure of Bi(111)," *Journal of Physics-Condensed Matter* **36** (2024). <https://doi.org/10.1088/1361-648X/acfb67>

23 A. Takayama, T. Sato, S. Souma, T. Oguchi, and T. Takahashi, "Tunable Spin Polarization in Bismuth Ultrathin Film on Si(111)," *Nano Letters* **12**, 1776-1779 (2012).
<https://doi.org/10.1021/nl2035018>

24 M. Wada, S. Murakami, F. Freimuth, and G. Bihlmayer, "Localized edge states in two-dimensional topological insulators: Ultrathin Bi films," *Physical Review B* **83** (2011).
<https://doi.org/10.1103/PhysRevB.83.121310>

25 Wilson J. Yáñez-Parreño, Alexander Vera, Sandra Santhosh, Chengye Dong, Jimmy C. Kotsakidis, Yongxi Ou, Saurav Islam, Adam L. Friedman, Maxwell Wetherington, Joshua

Robinson, and Nitin Samarth, "Charge-to-spin conversion in atomically thin bismuth," *Physical Review Applied* **23**, L061001 (2025). <https://doi.org/10.1103/fwrg-3dr2>

26 S. Murakami, "Quantum spin Hall effect and enhanced magnetic response by spin-orbit coupling," *Physical Review Letters* **97** (2006).
<https://doi.org/10.1103/PhysRevLett.97.236805>

27 I. Aguilera, H. J. Kim, C. Friedrich, G. Bihlmayer, and S. Blügel, "Z₂ topology of bismuth," *Physical Review Materials* **5** (2021). <https://doi.org/10.1103/PhysRevMaterials.5.L091201>

28 A. Canizo-Cabrera, E. Gómez-Barojas, C. Tabares-Muñoz, R. Silva-González, and V. García-Vázquez, "Figures of merit for niobium thin films grown on sapphire substrate," *Modern Physics Letters B* **15**, 639-642 (2001). <https://doi.org/10.1142/S021798490100218x>

29 H. L. Jia, B. Y. Zhou, T. Wang, Y. F. Wu, L. A. Yang, Z. Q. Ding, S. M. Li, X. Cai, K. L. Xiong, and J. G. Feng, "Investigation of the deposition of a-tantalum (110) films on a-plane sapphire substrate by molecular beam epitaxy for superconducting circuit," *Journal of Vacuum Science & Technology B* **41** (2023). <https://doi.org/10.1116/6.0002886>

30 A. P. M. Place, L. V. H. Rodgers, P. Mundada, B. M. Smitham, M. Fitzpatrick, Z. Q. Leng, A. Premkumar, J. Bryon, A. Vrajitoarea, S. Sussman, G. M. Cheng, T. Madhavan, H. K. Babla, X. H. Le, Y. Q. Gang, B. Jäck, A. Gyenis, N. Yao, R. J. Cava, N. P. de Leon, and A. A. Houck, "New material platform for superconducting transmon qubits with coherence times exceeding 0.3 milliseconds," *Nature Communications* **12** (2021).
<https://doi.org/10.1038/s41467-021-22030-5>

31 G. A. Prinz and J. J. Krebs, "Molecular-Beam Epitaxial-Growth of Single-Crystal Fe Films on Gaas," *Applied Physics Letters* **39**, 397-399 (1981). <https://doi.org/10.1063/1.92750>

32 C. L. Wang, X. G. Li, H. K. Xu, Z. Y. Li, J. H. Wang, Z. Yang, Z. Y. Mi, X. H. Liang, T. Su, C. H. Yang, G. Y. Wang, W. Y. Wang, Y. C. Li, M. Chen, C. Y. Li, K. H. Linghu, J. X. Han, Y. S. Zhang, Y. L. Feng, Y. Song, T. Ma, J. N. Zhang, R. X. Wang, P. Zhao, W. Y. Liu, G. M. Xue, Y. R. Jin, and H. F. Yu, "Towards practical quantum computers: transmon qubit with a lifetime approaching 0.5 milliseconds," *Npj Quantum Information* **8** (2022).
<https://doi.org/10.1038/s41534-021-00510-2>

33 Y. Guo, Y. F. Zhang, X. Y. Bao, T. Z. Han, Z. Tang, L. X. Zhang, W. G. Zhu, E. G. Wang, Q. Niu, Z. Q. Qiu, J. F. Jia, Z. X. Zhao, and Q. K. Xue, "Superconductivity modulated by quantum size effects," *Science* **306**, 1915-1917 (2004). <https://doi.org/10.1126/science.1105130>

34 C. Z. Xu, Y. H. Chan, Y. G. Chen, P. Chen, X. X. Wang, C. Dejoie, M. H. Wong, J. A. Hlevyack, H. J. Ryu, H. Y. Kee, N. Tamura, M. Y. Chou, Z. Hussain, S. K. Mo, and T. C. Chiang, "Elemental Topological Dirac Semimetal: a-Sn on InSb(111)," *Physical Review Letters* **118** (2017). <https://doi.org/10.1103/PhysRevLett.118.146402>

35 M. H. Vonhoegen, T. Schmidt, M. Henzler, G. Meyer, D. Winau, and K. H. Rieder, "Epitaxial Layer Growth of Ag(111)-Films on Si(100)," *Surface Science* **331**, 575-579 (1995).
[https://doi.org/10.1016/0039-6028\(95\)00320-7](https://doi.org/10.1016/0039-6028(95)00320-7)

36 V. B. Sandomirskii, "Quantum size effect in a semimetal film," *Physical Review B* **25**, 101 (1967).

37 Shunhao Xiao, Dahai Wei, and Xiaofeng Jin, "Bi (111) thin film with insulating interior but metallic surfaces," *Physical Review Letters* **109**, 166805 (2012).
<https://doi.org/10.1103/PhysRevLett.109.166805>

38 P. B. Alers and R. T. Webber, "The Magnetoresistance of Bismuth Crystals at Low Temperatures," *Physical Review* **91**, 1060-1065 (1953).
<https://link.aps.org/doi/10.1103/PhysRev.91.1060>

39 K. Behnia, L. Balicas, and Y. Kopelevich, "Signatures of electron fractionalization in ultraquantum bismuth," *Science* **317**, 1729-1731 (2007).
<https://doi.org/10.1126/science.1146509>

40 F. Y. Yang, K. Liu, K. M. Hong, D. H. Reich, P. C. Searson, and C. L. Chien, "Large magnetoresistance of electrodeposited single-crystal bismuth thin films," *Science* **284**, 1335-1337 (1999). <https://doi.org/10.1126/science.284.5418.1335>

41 Fucong Fei, Xiangyan Bo, Rui Wang, Bin Wu, Juan Jiang, Dongzhi Fu, Ming Gao, Hao Zheng, Yulin Chen, Xuefeng Wang, Haijun Bu, Fengqi Song, Xiangang Wan, Baigeng Wang, and Guanghou Wang, "Nontrivial Berry phase and type-II Dirac transport in the layered material PdTe₂," *Physical Review B* **96**, 041201 (2017). <https://doi.org/10.1103/PhysRevB.96.041201>

42 J. Fujioka, R. Yamada, M. Kawamura, S. Sakai, M. Hirayama, R. Arita, T. Okawa, D. Hashizume, M. Hoshino, and Y. Tokura, "Strong-correlation induced high-mobility electrons in Dirac semimetal of perovskite oxide," *Nature Communications* **10**, 362 (2019).
<https://doi.org/10.1038/s41467-018-08149-y>

43 Orest Pavlosiuk and Dariusz Kaczorowski, "Galvanomagnetic properties of the putative type-II Dirac semimetal PtTe₂," *Scientific Reports* **8**, 11297 (2018).
<https://doi.org/10.1038/s41598-018-29545-w>

44 Shen Zhang, Yibo Wang, Qingqi Zeng, Jianlei Shen, Xinqi Zheng, Jinying Yang, Zhaosheng Wang, Chuanying Xi, Binbin Wang, Min Zhou, Rongjin Huang, Hongxiang Wei, Yuan Yao, Shouguo Wang, Stuart S. P. Parkin, Claudia Felser, Enke Liu, and Baogen Shen, "Scaling of Berry-curvature monopole dominated large linear positive magnetoresistance," *Proceedings of the National Academy of Sciences* **119**, e2208505119 (2022).
<https://doi.org/10.1073/pnas.2208505119>

45 Charles Kittel and Paul McEuen, *Introduction to Solid State Physics*. (John Wiley & Sons, 2018).

46 Freeman Dyson, "A meeting with Enrico Fermi," *Nature* **427**, 297-297 (2004). 10.1038/427297a

47 Liang Fu, "Hexagonal Warping Effects in the Surface States of the Topological Insulator Bi₂Te₃," *Physical Review Letters* **103**, 266801 (2009). 10.1103/PhysRevLett.103.266801

48 Mallika T. Randeria, Benjamin E. Feldman, Fengcheng Wu, Hao Ding, András Gyenis, Huiwen Ji, R. J. Cava, Allan H. MacDonald, and Ali Yazdani, "Ferroelectric quantum Hall phase revealed by visualizing Landau level wavefunction interference," *Nature Physics* **14**, 796-800 (2018). 10.1038/s41567-018-0148-2

49 Eugene D. Ark et al. (unpublished), (2025).

50 K. Saito, H. Sawahata, T. Komine, and T. Aono, "Tight-binding theory of surface spin states on bismuth thin films," *Physical Review B* **93** (2016). 10.1103/PhysRevB.93.041301

51 J. Wang, A. M. DaSilva, C. Z. Chang, K. He, J. K. Jain, N. Samarth, X. C. Ma, Q. K. Xue, and M. H. W. Chan, "Evidence for electron-electron interaction in topological insulator thin films," *Physical Review B* **83** (2011). <https://doi.10.1103/PhysRevB.83.245438>

52 Shinobu Hikami, Anatoly I. Larkin, and Yosuke Nagaoka, "Spin-Orbit Interaction and Magnetoresistance in the Two Dimensional Random System," *Progress of Theoretical Physics* **63**, 707-710 (1980). <https://doi.org/10.1143/PTP.63.707>

Supplementary Material

Synthesis and transport properties of epitaxial Bi (111) films on GaAs (111) substrates

Jagannath Jena¹, Eugene D. Ark¹, Siddhesh Ambhire², Michael D. Smith¹, Justin S. Wood¹, Junyi Yang¹, John Pearson¹, Hanu Arava¹, Daniel Rosenmann³, U. Welp¹, J. S. Jiang¹, Deshun Hong¹, Ivar Martin¹, Steven S.-L. Zhang², and Anand Bhattacharya^{1*}

¹Material Science Division, Argonne National Laboratory, Lemont, Illinois 60439, USA

²Department of Physics, Case Western Reserve University, Cleveland, Ohio 44106, USA

³Center for Nanoscale Materials, Argonne National Laboratory, Lemont, Illinois 60439, USA

*anand@anl.gov

The Supplementary Material has 4 figures, Fig. S1 – S4, describing various aspects of the structural and transport properties of the films presented in the main text.

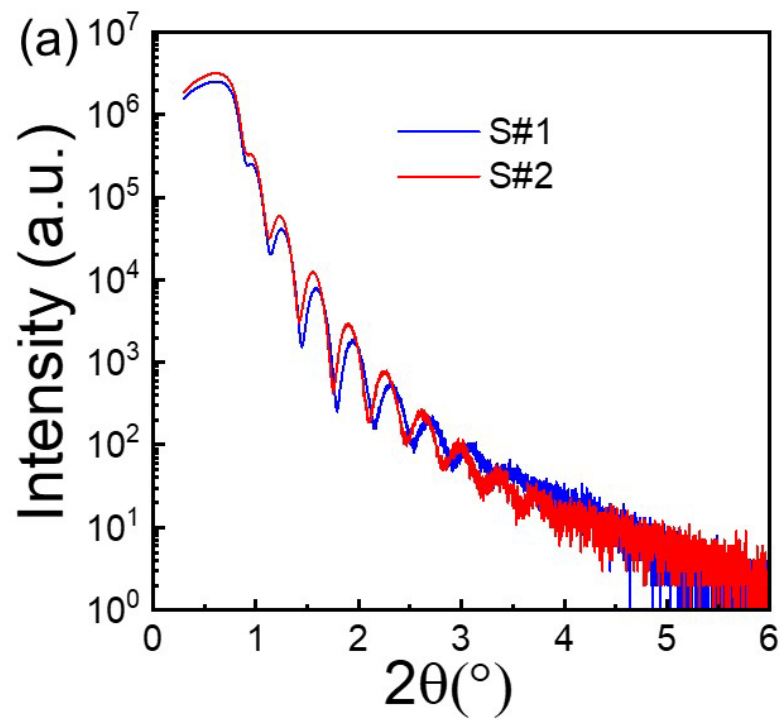


Figure. S1: (a) X-ray reflectivity (XRR) of 24 nm Bi (111) films on GaAs(111) substrate. Sample S#2 (red) exhibits a higher number of oscillations compared to S#1 (purple), indicating a smoother surface and/or film–substrate interface in S#2.

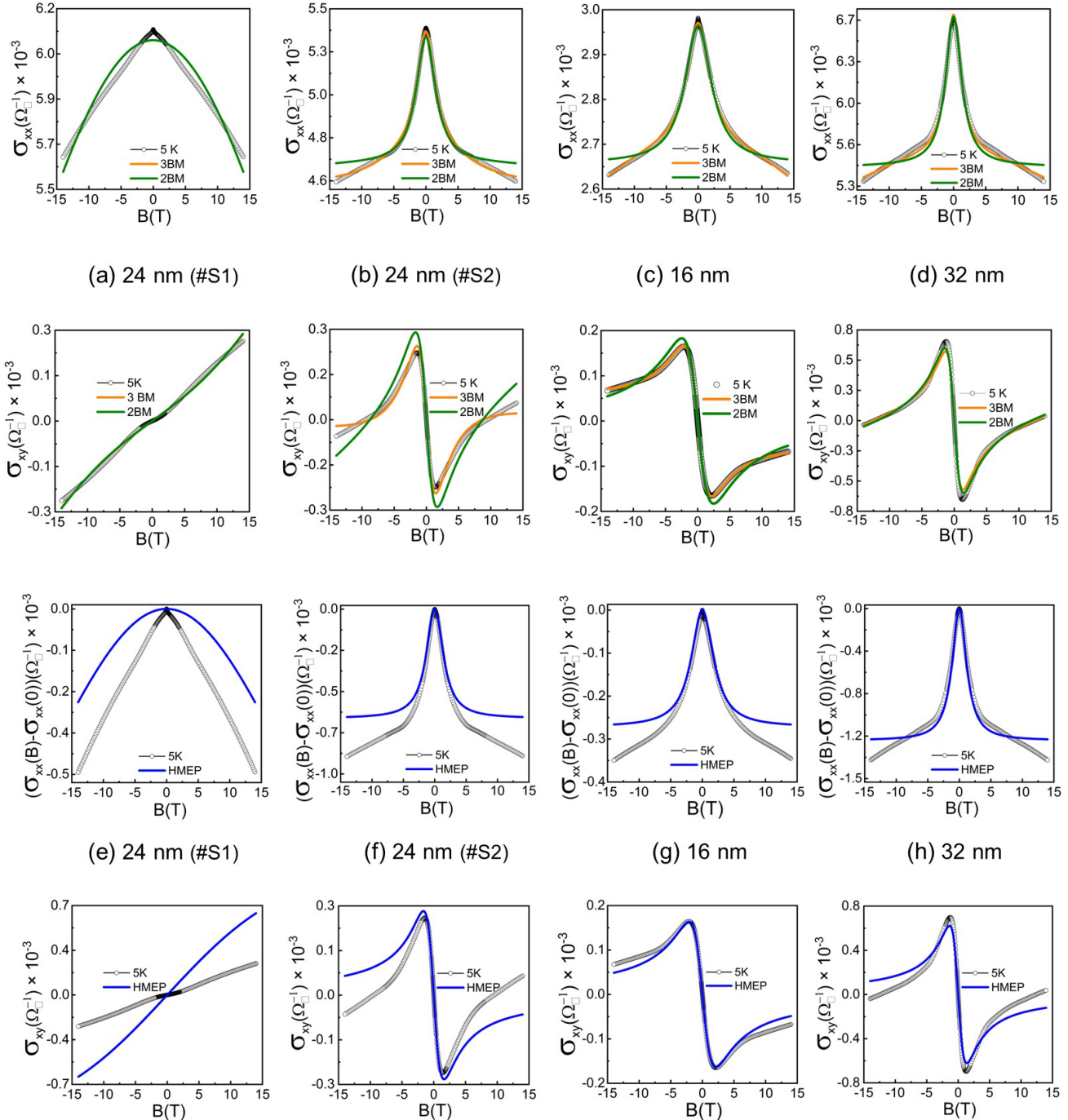


Fig. S2: (a-d) 3-Band and 2-Band fits to conductivity data for films of different thicknesses where σ_{xx} is shown in the upper panels and σ_{xy} in the lower panels. The 3-Band model yields a consistently better fit to the data. (e-f) Comparing the calculated conductivity for the high mobility band using parameters extracted from the 3-Band model to the measured data. The change in conductivity with B at all fields is dominated by the single high mobility band.

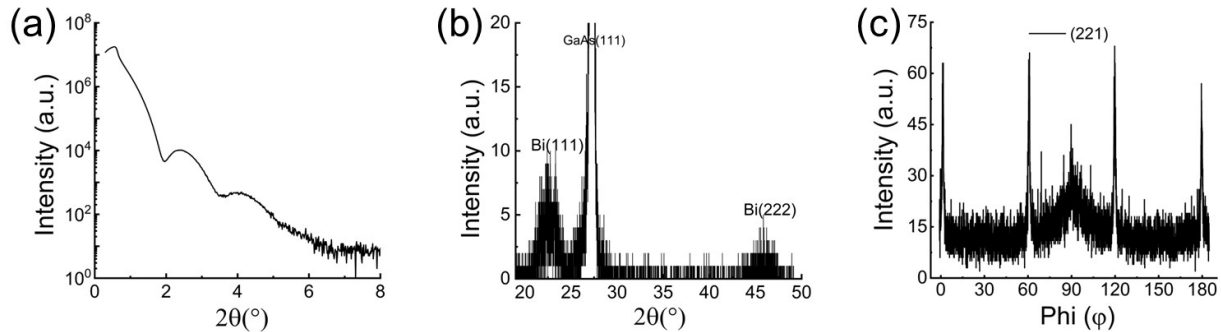


Figure S3: (a) X-ray diffraction (2-theta scan) – note peaks are indexed in hexagonal notation (b) X-ray reflectivity, and (c) Azimuthal (phi) scan using the $(10\bar{1}5)$ peak for the 5 nm Bi film.

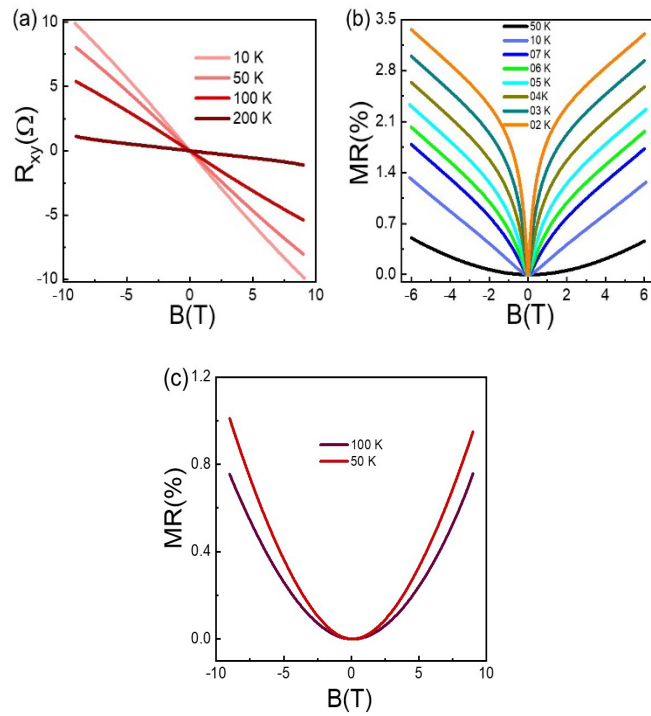


Figure. S4: (a) Hall resistance of a 5 nm Bi film measured at different temperatures: 10 K, 50 K, 100 K, and 200 K. (b) Magnetoresistance (MR) of the 5 nm Bi (111) film showed a cusp-like behavior with positive MR—indicative of weak anti-localization (WAL)—which is more pronounced at low temperatures and gradually diminishes at higher temperatures. (c) At elevated temperatures (50 K and 100 K), the MR curves showed a parabolic shape, characteristic of classical magnetoresistance.